Emergence of anomalous dynamics in soft matter probed at the European XFEL – Supporting Information

Felix Lehmkühler,[1,2,3,*] Francesco Dallari,[1,†] Avni Jain,[1,†] Marcin Sikorski,[4] Johannes Möller,[4] Lara Frenzel,[1,2] Irina Lokteva,[1,2] Grant Mills,[4] Michael Walther,[1] Harald Sinn,[4] Florian Schulz,[2,5] Michael Dartsch,[1,2] Verena Markmann,[1] Richard Bean,[4] Yoonhee Kim,[4] Patrik Vagovic,[6,4] Anders Madsen,[4] Adrian P. Mancuso,[4,7] and Gerhard Grübel[1,2,3]

[1] *Deutsches Elektronen-Synchrotron DESY, Notkestr. 85, 22607 Hamburg, Germany*

[2] *The Hamburg Centre for Ultrafast Imaging, Luruper Chaussee 149, 22761 Hamburg, Germany*

[3] *Center for Molecular Water Science (CMWS), Notkestr. 85, 22607 Hamburg, Germany*

[4] *European XFEL, Holzkoppel 4, 22869 Schenefeld, Germany*

[5] *Institute for Physical Chemistry, University of Hamburg, Grindelallee 117, 20146 Hamburg, Germany*

[6] *Center for Free-Electron Laser Science, Deutsches Elektronen Synchrotron DESY, Notkestr. 85, 22607 Hamburg, Germany*

[7] *Department of Chemistry and Physics, La Trobe Institute for Molecular Science, La Trobe University, Melbourne, Victoria, 3086, Australia*

(Dated: September 4, 2020)

This Supporting Information contains information on the pulse intensity over the pulse trains, details on the data analysis, further measurements and a calculation of speckle contrast, and the model to describe the temperature increase of the probed samples.

* Corresponding author: felix.lehmkuehler@desy.de

† These two authors contributed equally

www.pnas.org/cgi/doi/10.1073/pnas.2003337117

I. PULSE INTENSITY

The intensity of each single pulse is measured by a gas monitor upstream the sample position. The values are given in Supporting Figure S1 for one run consisting of 500 trains. During the experimental run on those samples, the pulse intensity showed on average a maximum around pulse number 40 and decreased values at larger pulse numbers. Note that this may slightly differ for different trains and machine operation conditions. We used silicon crystals of different thickness to attenuate the intensity [1] and limit the radiation exposure of the samples, which are located between the gas monitor and the sample. The X-ray fluence on the sample was calculated by the pulse intensity shown in Supporting Figure S1, corrected for the beamline transmission and the transmission through the attenuator crystals. Throughout the paper average pulse fluences are used to label the runs (i.e. between 1.5 and 56.8 mJ/mm^2). The exact intensity value within the pulse train was used for modelling the temperature increase (see below).

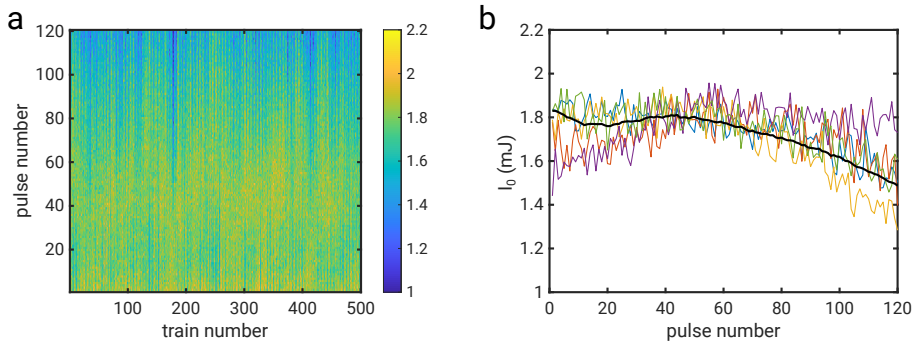

Supporting Figure S1. (a) Pulse intensity measured by the gas monitor upstream the sample position for one run on the dynamic sample. Colorscale is in mJ. (b) Pulse intensity for trains 1, 101, 201, 301, and 401 from (a) and average (black line) over 500 trains.

II. DATA ANALYSIS

The data were collected using the data acquisition system of the European XFEL [2] and the AGIPD available at the SPB/SFX beamline [3]. The AGIPD consists of 16 modules composed of 512×128 pixels with a size of 200×200 μm^2. It is capable of acquiring images with MHz frame rates, and each pixel electronics can automatically switch among three different gain settings – low, medium and high- depending on the incident value of the photon signal on the pixel. In the experiment performed here, all the data were collected in the high gain mode. Uncalibrated data files in the European XFEL format were used and detector calibration was done using in-house developed codes. Data from each AGIPD module was saved into separate files consisting of chunk sizes of 256 trains. A full image was constructed from the 16 modules by matching the data from the same train and pulse number. The following calibration steps were performed to obtain a speckle pattern for XPCS analysis. Firstly, a high-gain pedestal correction calculated as an average of 500 trains from the high-gain dark data set - was applied to each pixel for each pulse ID. Secondly, bad pixels were identified from the dark data set as those having ADU (analog-to-digital unit) values and standard deviation outside the statistically valid range. We also omitted specific pulse IDs within a train which displayed faulty electronic behavior (pulse numbers 18, 31, 50, 82, 114 correspond to bad memory cells of the detector), limiting ourselves to 114 pulses from a total of 120 pulses within a single train. The set of bad pixels from each of the 114 pulses were merged to form a mask that was applied to a single shot for the SAXS and XPCS calculations. For the calculations performed here, the percentage of masked pixels ranged between 7% and 28% for the studied regions of interest (same q). Lastly, we performed a baseline correction to refine the position of the zero-photon peak by subtracting the intensity values of each pixel in a module by the corresponding median value of a dark region (defined by 128×128 pixels) at the outer edge of that module.

To gain a precise mapping of pixel to wave vector transfer q value, the detector geometry was fine-tuned by calculating the azimuthally averaged intensity $I(q)$ from each of the four quadrants of the AGIPD for the static sample. The direct beam position was optimized such that the intensity profiles obtained from each quadrant are indistinguishable from each other. This criterion is valid as intensity scattered by uniformly distributed spherical nanoparticles have to be invariant under rotation symmetries. With the calibrated full-image data and refined detector geometry, we evaluated the $I(q)$, the single shot contrast and the intensity correlation functions $C(n_p, n_p + n)$ as well as the intensity autocorrelation functions $g_2(q, \tau)$. The latter two quantities are calculated

for a single train and then averaged over all trains to produce the curves in Fig. 3 and Fig. 4. For the definition of n_p see Supporting Figure S5. The $g_2(q, \tau)$ is carefully tracked for each individual train to follow the sample's response to the total accumulated radiation dose in the sample (i.e., we consider each train of pulses as an independent measurement).

III. SPECKLE CONTRAST

A. Stability over pulse trains

The single-shot speckle contrast is given by the normalized variance of intensity $I(q)$ [4, 5]

$$\beta_s(q) = \frac{\langle I(q)^2\rangle - \langle I(q)\rangle^2}{\langle I(q)\rangle^2} - \frac{1}{\langle k(q)\rangle}, \tag{1}$$

where $\langle k(q)\rangle$ denotes the average photon counts at wave vector transfer q. In order to determine the stability of the speckle contrast over the pulse trains, we calculated the average speckle contrast obtained from the static sample. The result is shown in Supporting Figure S2 (a) for 100 subsequent pulses. Here, the average contrast is 0.228, with an average relative variation $v = \mathrm{std}(\beta_s)/\langle\beta_s\rangle = 0.07$ over the pulse train, see Supporting Figure S2 (b).

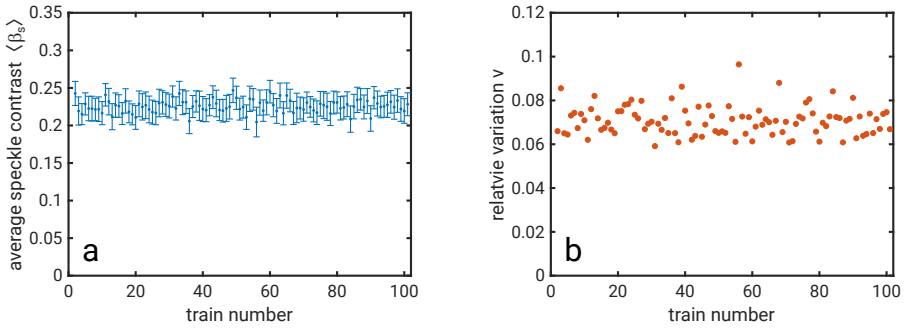

Supporting Figure S2. (a) Average speckle contrast from 100 trains at $q = 0.22$ nm^{-1}. The values were averaged over 114 pulses from each train, the errorbars are the standard deviation of the contrast over the train. (b) Relative variation v of the speckle contrast for the data shown in (a).

B. Calculation of speckle contrast and degree of transverse coherence

In SAXS experiments, the speckle contrast is typically given by the transverse coherence of the X-ray beam. However, due to a better signal-to-noise ratio, the speckle size is typically chosen to be similar to the size of a detector pixel [6] which leads to a reduced speckle contrast that can be modeled by geometry corrections [7]. This can be overcome when the speckles are oversampled, i.e., pixel sizes are much smaller compared to the speckle size [8, 9]. For pink beam SAXS experiments as in this work, the influence of the longitudinal coherence on the speckle contrast cannot be neglected. Compared to monochromatized X-ray beams, typically used at storage ring sources, the longitudinal coherence length is reduced leading to a q-dependence of the experimental speckle

contrast. In such cases the speckle contrast and the coherence factor can be approximated using different corrections [10–12]. Here, we used the approximation introduced by Hruszkewycz et al. [11] which has been successfully applied for FEL data from LCLS. In this context, the measured speckle contrast is given by $\beta_{\mathrm{exp}} = \beta_t \beta_\ell$, where β_t is the effective speckle contrast due to the transverse coherence given by the coherence factor $c = \sqrt{\beta_t}$. β_ℓ denotes the correction for energy bandwidth, experiment geometry, and speckle shape. This correction is given by $\beta_\ell = (M_{\mathrm{rad}} M_{\mathrm{det}})^{-1}$. The factor M_{rad} is given by

$$M_{\mathrm{rad}} = \sqrt{1 + \frac{q^2 (\Delta E/E)^2 [b_s^2 \cos^2(\theta) + t^2 \sin^2(\theta)]}{4\pi^2}} \tag{2}$$

accounting for the energy bandwidth $\Delta E/E \approx 5 \times 10^{-3}$, sample thickness t, and beam size b_s. The correction due to the pixel size of the detector and speckle size is

$$M_{\mathrm{det}} = \sqrt{1 + \frac{p^4 b_s^2 [b_s^2 \cos^2(\theta/2) + t^2 \sin^2(\theta/2)]}{\lambda^4 L^4 M_{\mathrm{rad}}^2}}, \tag{3}$$

with the pixel size $p = 200$ μm and sample-detector distance $L = 5.5$ m. In this way we obtained $\beta_t = \beta_{\mathrm{exp}}/\beta_\ell = 0.504$ used for the solid line in Fig. 2 (b) in the article modelling β_{exp}. This relates to an average degree of transverse coherence of $c = \sqrt{\beta_t} = 0.71 \pm 0.03$, which is similar to results from other hard X-ray FEL facilities [9, 13].

IV. ADDITIONAL XPCS RESULTS

In Supporting Fig. S3 XPCS results from low fluence data at $H = 3.9$ mJ/mm^2 are shown. Despite the reduced statistics, g_2-functions can be obtained from single trains (Supporting Fig. S3 (a)). Furthermore, the instantaneous correlation function C does not show neither broadening or narrowing over the pulses. This indicates that the sample was stable, in particular it implies a stable effective temperature without successive heating.

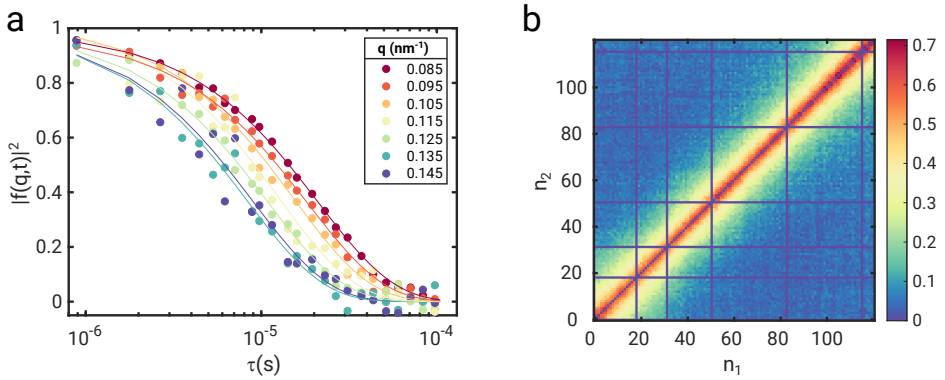

Supporting Figure S3. (a) Single-train g_2 functions at different q-values for $H = 3.9$ mJ/mm^2. (b) Instantaneous correlation function $C(n_1, n_2) = C(n_p, n_p + n)$ for $q = 0.125$ nm^{-1} and $H = 3.9$ mJ/mm^2. Due to limited statistics, C is average over 500 pulse trains.

The g_2-functions averaged over 500 pulse trains are shown in Supporting Fig. S4 for $H = 27.7$ mJ/mm^2 and $H = 3.9$ mJ/mm^2. The data in Supporting Fig. S4 (a) complements the single-train data shown in Fig. 3 (b) in the main text, the results in Supporting Fig. S4 (b) corresponds to the single-train data in Supporting Fig. S3 (a).

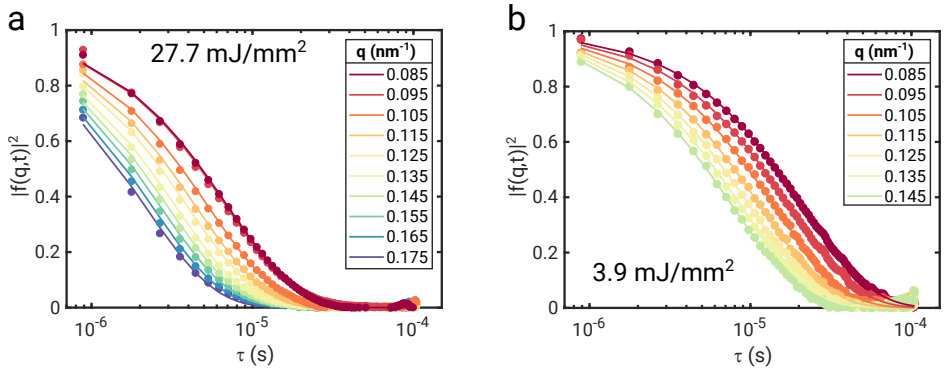

Supporting Figure S4. Averaged g_2-functions for (a) $H = 27.7$ mJ/mm^2 and (b) $H = 3.9$ mJ/mm^2.

V. HEATING MODEL

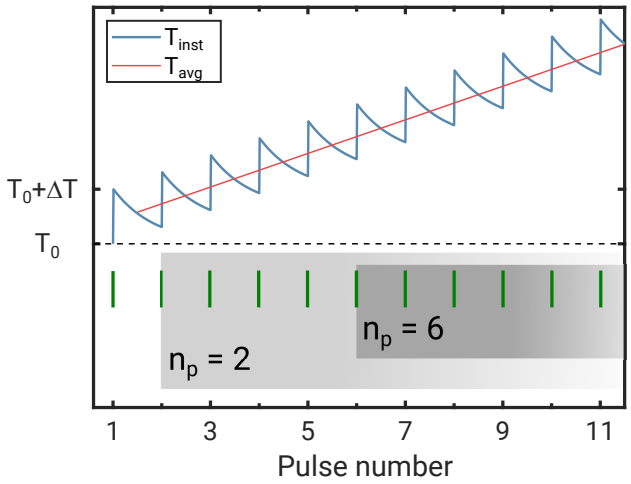

Supporting Figure S5. Schematic heat increase and definition of n_p. The instantaneous temperature T_{inst} and the temperature averaged between two pulses T_{avg} are shown schematically. T_0 is the start temperature, ΔT denotes the maximum temperature just after the X-ray pulse. The green bars mark the pulses.

After the X-ray pulses hit the sample, the sample temperature increases on short time scales due to absorption of X-ray photons. Afterwards, the temperature relaxes on time scales defined by the thermodynamic properties of the sample. These time scales are typically in the range of microseconds using micrometer-sized X-ray beam and have to be considered for microsecond-XPCS. A general scheme is shown in Supporting Figure S5, where after each pulse the system's temperature increases sharply and tries to relax back to equilibrium. However, since the time separation is not enough for a complete relaxation, the average temperature will steadily increase with the number of pulses. We can define then n_p as the first pulse from where the correlation function has been calculated. For instance, for $n_p = 6$ the first 5 pulses of the pulse train represent pump pulses only, that heat up the sample. The first correlation is calculated between speckle patterns measured with the 6th and 7th pulse. Consequently, we assume for $n_p = 6$ in total 6 pump pulses, followed by $120 - n_p$ probe pulses, which naturally continue to heat up the sample.

This situation is similar to the one described by the HBM model but with a crucial difference: the heat source (i.e. the X-ray pulses) is not stationary in time, therefore we lose one of the fundamental hypothesis over which the HBM is built [14]. We can then describe our data with a slightly less approximate picture considering the total temperature increase and relaxation of the sample is considered as a combination of (1) the heating of the solvent (water) due to absorption of X-rays and (2) the heating of and successive heat transfer from the silica nanoparticles to the

surrounding water volume.

A. Water heating

For an idealized Gaussian intensity distribution, the temperature distribution in the material after a single X-ray pulse hitting the sample at normal incidence is given by

$$\Delta T(r,z) = \Delta T_{\max} \exp\left(-\frac{r^2}{2\sigma^2} - \frac{z}{\lambda_{abs}}\right), \tag{4}$$

where r is the radial distance from the beam axis and z is the distance from the sample's surface along the beam direction. $\Delta T_{\max}$ is the maximum of the temperature distribution function on the surface and can be calculated as:

$$\Delta T_{\max} = \frac{E_{pulse}}{2\pi c_p \rho \sigma^2 \lambda_{abs}/(4\ln(2))}$$

where E_{pulse} = denotes the pulse energy on the sample, $c_p = 4.186$ J/gK the heat capacity of water, $\rho = 1$ g/cm^3 water's mass density, $\lambda_{abs} = 1570$ μm the absorption length of X-rays at 9.3 keV, and σ the beam size.

For low-Z materials that have long X-ray absorption length for hard X-rays compared to the beam size, the dominant heat flow will point radially away from the beam axis and the dependence on z can be neglected. For a δ-like initial heat distribution, the time evolution of the temperature is described by the Gaussian widening with the square root of time:

$$\Delta T(r,t') \propto \frac{t_0}{2\pi\sigma^2 t'} e^{-\frac{r^2}{2\sigma(t')^2}} = \frac{c_p\rho}{4\pi k_W t'} e^{-\frac{c_p\rho r^2}{4k_W t'}},$$

with the heat conductivity of water k_W. We define a time t_0, where the δ-like initial distribution has relaxed to the width of the impinging Gaussian beam:

$$t_0 = \frac{c_p\rho\sigma^2}{2k_W}. \tag{5}$$

The time t that describes the time evolution after the initial beam profile is defined by $t' = t + t_0$. This leads to

$$\Delta T(r,t) \propto \frac{1}{2\sigma^2(1+t/t_0)} \exp\left(-\frac{r^2}{2\pi\sigma^2(1+t/t_0)}\right).$$

The proportionality constant is chosen such that initial temperature is correct:

$$\Delta T(r,t) = \frac{\Delta T_{\max}}{(1+t/t_0)} \exp\left(-\frac{r^2}{2\sigma^2(1+t/t_0)}\right).$$

After n pulses with a separation δt the heat profiles for different time evolutions are added up, leading to a peak temperature of:

$$T_n = \Delta T_{\max} \sum_{n=0}^{N} \frac{1}{1 + (n\delta t/t_0)} + T_0.$$

From the expression of $\Delta T(r,t)$ we can obtain the average temperature of the Gaussian distribution in a given volume $V = \pi L \sigma^2$:

$$\Delta T(t) = \frac{1}{\pi L \sigma^2} \int_{2\pi} d\phi \int_L dz \int_0^{\sigma^2} \frac{\Delta T_{\max}}{(1 + t/t_0)} \exp\left(-\frac{r^2}{2\sigma^2(1 + t/t_0)}\right) r dr$$

$$\Delta T(t) = \Delta T_{\max} \left[1 - \exp\left(-\frac{1}{2(1 + t/t_0)}\right)\right].$$

Thus, the temperature increment after N pulses is:

$$\Delta T_N = \Delta T_{\max} \sum_{n=0}^{N} \left[1 - \exp\left(-\frac{1}{2(1 + (n\delta t)/t_0)}\right)\right],$$

generalizing to a fluctuating pulse intensity one gets:

$$\Delta T_N(t) = \sum_{n=0}^{N} \Delta T_{\max}^{(n)} \left[1 - \exp\left(-\frac{1}{2(1 + (t + (N-n)\delta t)/t_0)}\right)\right] \tag{6}$$

Both for the peak and average temperature the timescale of the thermal relaxation is described by t_0 (see Eq. 5), which in our system is $t_0 \sim 56\mu$s. Since water is nearly transparent for the hard X-rays, its temperature increase per pulse is small but cannot be dissipated in 886 ns, before the next pulse hits the sample. Thus, the time evolution of the water temperature will be a series of small steps as shown in Supporting Figures S5 and S6.

B. Silica nanoparticles

The density and the relative number of absorbed photons are higher for the silica particles compared to water (leading to a higher temperature increase per pulse). However, their small size makes their thermal relaxation much faster. The temperature increase of a single nanoparticle of radius $R = 70$ nm is:

$$\Delta T_{\max}^{\mathrm{SiO2}} = \frac{\frac{E_{pulse}}{\sigma^2}\sigma_{\mathrm{NP}}^2}{c_p^{\mathrm{SiO2}} \rho_{\mathrm{SiO2}} v_{\mathrm{SiO2}}},$$

where $c_p^{SiO2} = 0.737$ J/gK is the heat capacity, $\rho = 2.1$ g/cm^3 the density of colloidal silica (Note: colloidal silica is slightly less dense than bulk), $v_{\mathrm{SiO2}} = (4/3)\pi R^3$), $\sigma_{\mathrm{NP}}^2 = (\mu/\rho) \times m =$

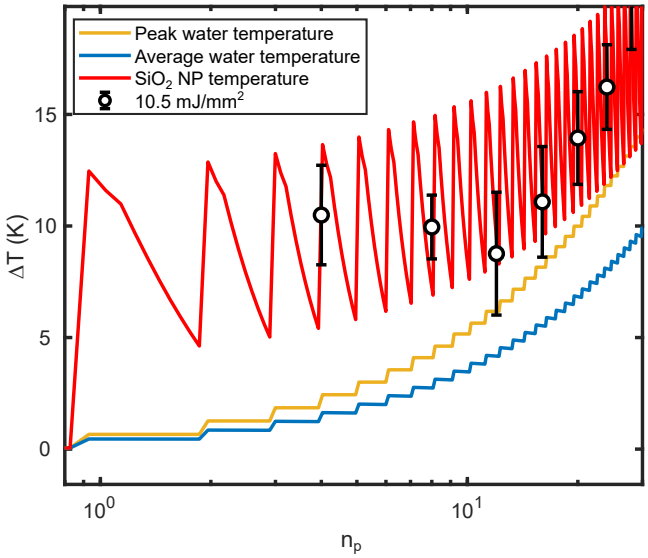

Supporting Figure S6. Temperature evolution of water following Eq. 6 and silica particles for an X-ray pulse fluence of 10.5 mJ/mm^2. For clarity, data is shown as a function of n_p. For water, the peak temperature after each pulse as well as the average temperature over the scattering volume are shown. Data points from Fig. 4 in the main text are shown for comparison.

$(\lambda_{abs}^{\mathrm{SiO2}}\rho)^{-1}\rho \times v_{\mathrm{SiO2}} = v_{\mathrm{SiO2}}/\lambda_{abs}^{\mathrm{SiO2}}$ denotes the cross-section, and $\lambda_{abs}^{\mathrm{SiO2}} = 223.721\mu$m the absorption length.

The temperature within nanoparticle can be described as

$$\Delta T(r,t)^{SiO2} = \sum_i \frac{4(\sin(\lambda_i) - \lambda_i \cos(\lambda_i))}{2\lambda_i - \sin(\lambda_i)} \frac{\sin(\lambda_i r/R)}{\lambda_i r/R} e^{-\lambda_i^2 \frac{\alpha}{R^2} t}, \qquad r \in [0, R] \tag{7}$$

where λ_i are the roots of the equation

$$1 - \lambda_i \cot(\lambda_i) = Bi$$

and

$$\alpha = \frac{k}{\rho c_p} \qquad Bi = hR/k,$$

Here, $k \sim 1.39$ W/mK [15] and h is the convective heat transfer coefficient from water with values in the range of $10^2 - 10^4$ J/sm^{2}K (table 2.2 from `https://personalpages.manchester.ac.uk/staff/tom.rodgers/documents/HT_Notes.pdf`).

The heat transfer between the silica nanoparticle and the surrounding water is governed by the Biot number Bi, which is proportional to $R \sim 7 * 10^{-8}$m and much smaller than 1 for every allowed value of h (in the range 10^2 to 10^4 J/sm^{2}K). Values of $Bi \ll 1$ imply a negligible temperature

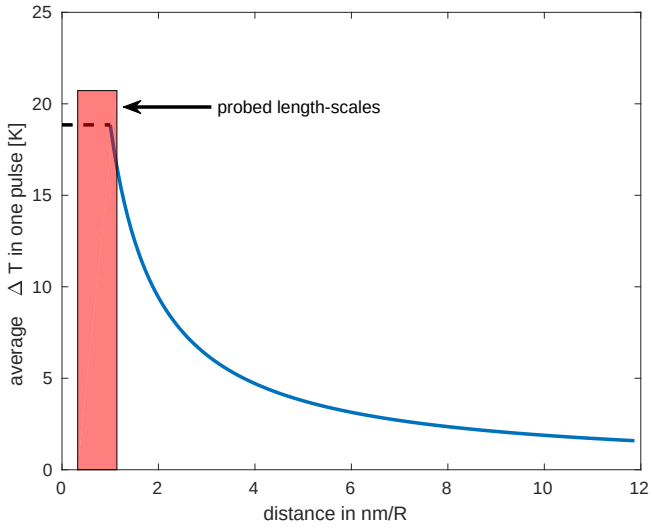

Supporting Figure S7. Average temperature jump for $H = 27.7$ mJ/mm^2 between two pulses as a function of the distance from the center of the nanoparticle. The red area markes the typical length scale probed related to the experimental q-resolution.

gradient inside the nanoparticle. Thus, we can approximate a single sphere as a lump of matter at a given temperature and describe the temperature of the surrounding water with the profile

$$T^{\mathrm{SW}}(R,t) = \frac{\Delta T^{\mathrm{SiO2}}(R,t)}{r/R} + T^{\mathrm{SW}}(r \to \infty, t = 0), \qquad r > R.$$

This reduces in Newton's approximation to:

$$\Delta T(r,t)^{SW} = \frac{\left(\Delta T^{SiO2}_{max}\right) e^{-3\frac{k}{k_w} Bi \frac{\alpha}{R^2} t}}{r/R}, \qquad r > R. \tag{8}$$

The results are shown in Supporting Figures S7 and S8 using the parameters of the experiment.

C. Time-dependent heating model

In our time-dependent model we assume nanoparticles initially at the same temperature of the surrounding water. After the absorption of the X-ray pulse, the particles heat up and begin to relax back towards the solvent temperature. Depending on the value of Bi, the particles will relax completely to the water temperature or will stay slightly heated.

Since the probed time scales are comparable with the characteristic time of the thermal relaxation of a single nanoparticle, and the length scales are limited to few nanometers, the measured "effective temperature" from the correlation function g_2 is determined by the local temperature of the thin layer of water surroundings the nanoparticles. Thus, after a single pulse the detected

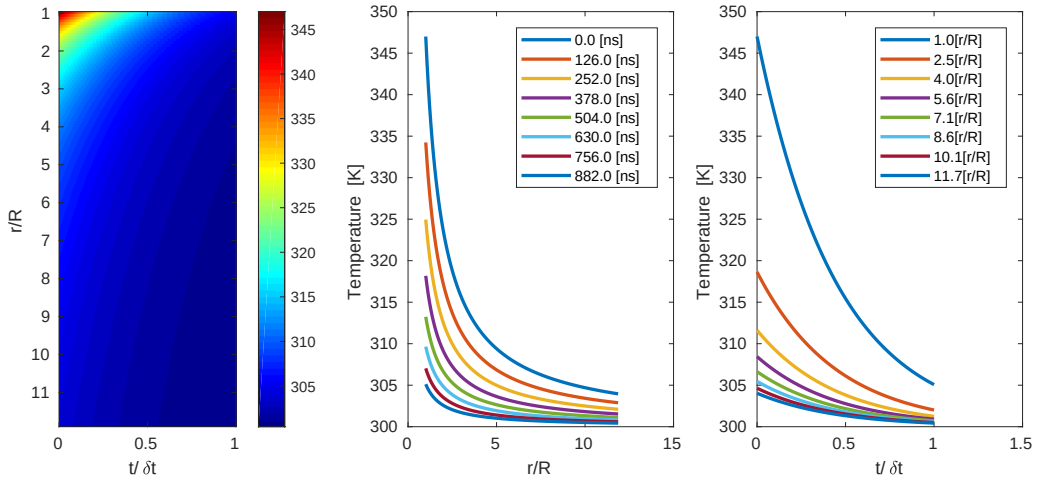

Supporting Figure S8. left: $T(r,t)$ calculated over distances up to the average particle-particle separation, and in the time interval between two pulses. Center: $T(r)$ at fixed times; right: $T(t)$ at fixed distances.

temperature in the boundary layer can jump a few tens of degrees even if the temperature of the water a few molecular distances further is essentially unchanged. A stretching exponent $\gamma < 1$ appears only with the stronger pulse intensities and it decrease further as a function of the number of pulses. A decrease in γ reflects typically increasing heterogeneity, likely originating from temperature heterogeneities.

Despite the fact that after each pulse the nanoparticles can become extremely hot, the real temperature of the probed volume is mostly determined by the heat deposited directly in the water described by Eq. 6. In fact, the ratio between the heat capacities of silica nanoparticles and water is $\sim \Phi c_p^{SiO2}/c_p^{H2O} \sim 0.0033$, with $\Phi \sim 2\%$ mass concentration, so that the heat collected by the nanoparticles is negligible in comparison to the whole scattering volume.

The effective temperature was extracted from the relaxation rates Γ as outlined in the main text. Using the Stokes-Einstein relation, the relaxation rate is given by

$$\Gamma = Dq^2 = \frac{k_\mathrm{B}}{6\pi R} \cdot \frac{T}{\eta(T)}. \tag{9}$$

The temperature dependence lies thus in the term $T/\eta(T)$. Relaxation rates extracted from correlation functions $C(n_p, n_p + n)$ for different n_p and at $q = 0.125$ nm^{-1} are shown in Supporting Figure S9 (a) as a function of n_p. These and Γ at the other q-values measured were used to obtain the effective temperature shown in Fig. 4 (c).

The heat model is visualized in Supporting Figure S9 (b). Therein, the temperature increase measured for $H = 27.7$ mJ/mm^2 as a function of n_p is compared to the average temperature

increase of the solvent water, the silica nanoparticle, and to the time-dependent model taking heat transfer from the nanoparticle to the surrounding water volume into account. Since the heat of the nanoparticles relaxes on a shorter time scale than for water, the pulse lead to an effective temperature increase that does not vary significantly over the pulse train. Due to the drop of intensities with pulse number (see Supporting Figure S1), the temperature of the nanoparticles slightly reduces for large n_p. In contrast, water experiences a steady increase of temperature because of the much slower temperature relaxation times. Consequently, the initial temperature increase reported in Fig. 4 of the main text is dominated by the nanoparticles, while the behavior at longer times is dominated by the temperature increase of water. Furthermore, the model is compared to the model of a hot diffusing nanoparticle in a simple liquid [14]. Therein, diffusion is described by a modified Stokes-Einstein relation, where the temperature and viscosity are replaced by effective values. For temperature increases smaller than the starting temperature, the effective temperature for hot diffusion T_{HBM} can be approximated by a Taylor expansion [14]

$$T_{\mathrm{HBM}} = T_0 + \Delta T_{\mathrm{NP}}/2 - [1 - \ln(\eta_0/\eta_\infty)]\Delta T_{\mathrm{NP}}^2/(24T_0). \tag{10}$$

Here, T_0 is the solvent temperature where we use the temperature from the water model (blue line in Supporting Figure S9 (b)), ΔT_{NP} is the temperature difference between the nanoparticles and the water (red line), η_0 is the viscosity of water at T_0 and $\eta_\infty = 0.0298$ mPa·s [14]. In addition, an effective viscosity η_{HBM} is defined following [14], leading to an effective diffusion constant

$$D_{\mathrm{HBM}} = \frac{k_{\mathrm{B}} T_{\mathrm{HBM}}}{6\pi\eta_{HBM} R}. \tag{11}$$

The viscosities from the HBM model and water heating are shown in Supporting Figure S10 (a) for $H = 56.8$ mJ/mm^2. In Supporting Figure S10 (b) the diffusion coefficient is shown for $H = 56.8$ mJ/mm^2 together with the time-dependent model and HBM model as shown in Figure 4 of the main text.

The non-linear heating mechanism is further highlighted by studying the dependence of the relaxation rate Γ as a function of H at fixed n_p (i.e., vertical cuts through Supporting Figure S9 a). The results are shown in Supporting Figure S11 (a) for five values of n_p. The data were modeled by exponential functions

$$\Gamma(H) = a \exp(bH), \tag{12}$$

which roughly follows the expected change of Γ with temperature (see Eq. 9). The growth rate b is shown in Supporting Figure S11 (b). We observe a constant value of b at low n_p, where the

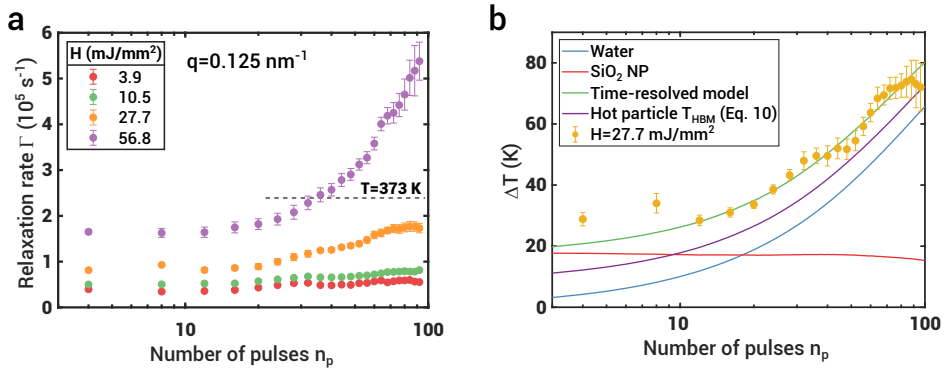

Supporting Figure S9. a) Relaxation rate Γ as function of pulse number in the pulse train n_p for different H. The data shown was measured at $q = 0.125$ nm^{-1}. b) Temperature increase as a function of n_p. The data taken for $H = 27.7$ mJ/mm^2 are compared to the heating of water as solvent (blue), the heating of the individual nanoparticles (NP, red), the time-dependent model where the NP transfer heat to the surrounding water volume (green), and the model of hot diffusing particles (purple) [14].

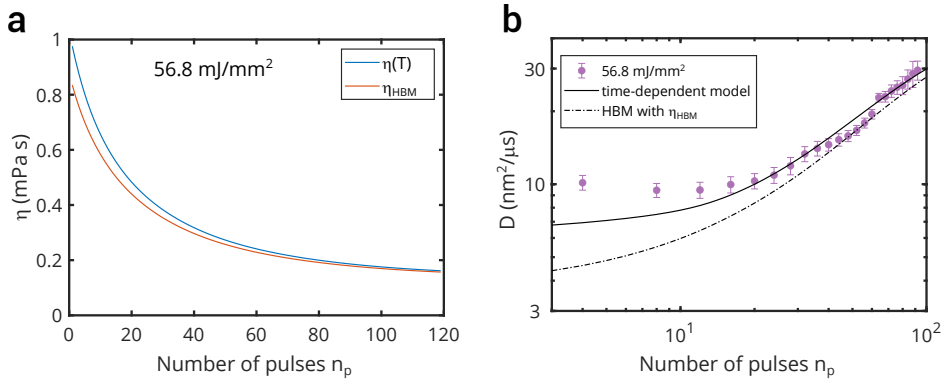

Supporting Figure S10. a) Viscosities of water from [16] and from HBM model for $H = 56.8$ mJ/mm^2. b) Diffusion coefficient for $H = 56.8$ mJ/mm^2 compared to the time-dependent model and the HBM model using η_{HBM} (dashed-dotted line) and $\eta(T)$ with $T = T_{\mathrm{HBM}}$ (dashed line).

heating of the nanoparticle dominates leading to a constant temperature. This is in agreement with the results from Fig. 4 d, where the temperature does not change significantly up to $n_p \approx 20$. For larger values of n_p, the growth rate b increases significantly where the heating of the solvent dominates. The contribution of the heating of the nanoparticles and the solvent are highlighted by the solid lines representing the different models as discussed in Supporting Figure S9.

As a consequence of the non-linear heating, the dynamics become heterogeneous. This can be quantified by the Kohlrausch-Williams-Watt (KWW) exponent γ that becomes less than 1.

Fits to the correlation functions $C(n_p, n_p + n)$ are shown in Supporting Figure S12. Here, we compare fits to a single exponential $f(q, \tau) = \exp(-\Gamma\tau)$ with fits to the KWW function $f(q, \tau) =$

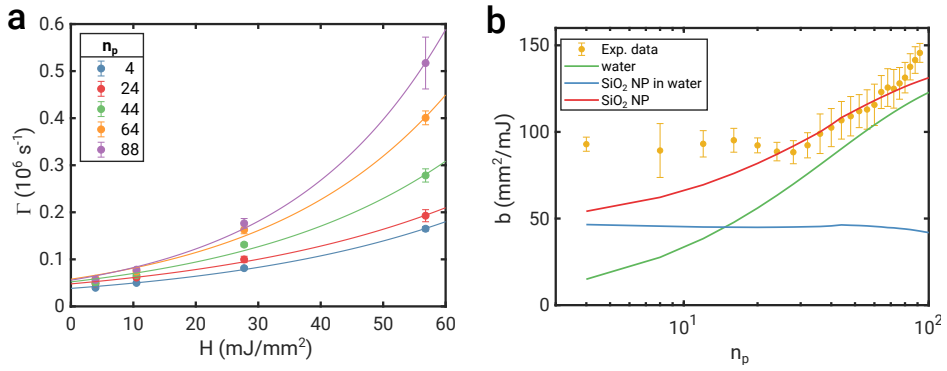

Supporting Figure S11. (a) Relaxation rate Γ as a function of H. The lines are fits to the exponential function (Eq. 12). (b) Growth rate b from Eq. 12 together with the growth rate calculated from the heating models.

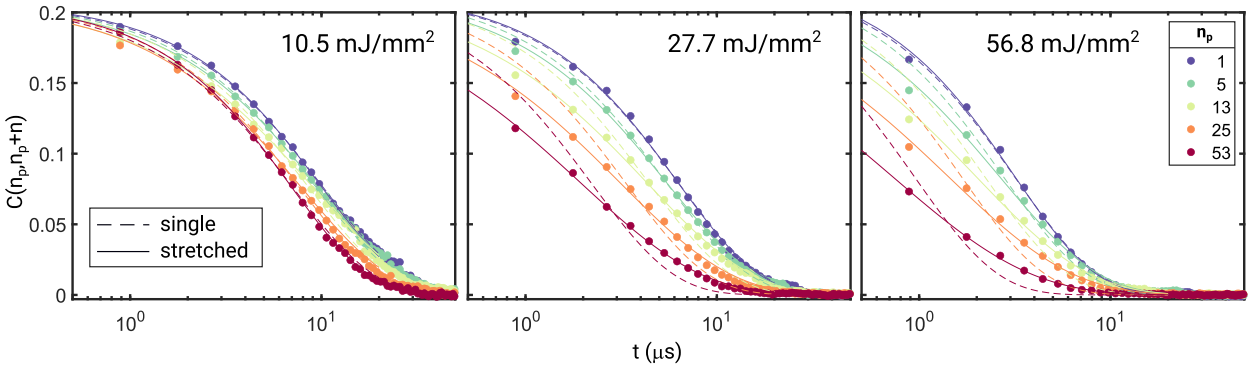

Supporting Figure S12. Correlation functions $C(n_p, n_p + n)$ for $q = 0.125$ nm^{-1} and the three highest fluences. Fits using (i) a single exponential (dashed lines) and (ii) stretched exponential (solid lines) are compared.

$\exp(-[\Gamma\tau]^\gamma)$ (Eq. 3) in the main text. The speckle contrast has been fixed to the result obtained from the static samples as described in the main text. For $H = 10.5$ mJ/mm^2 we typically obtain $\gamma \approx 1$, indicating a single-exponential relaxation. In contrast, for the two highest fluences, the single exponentials only model the data well for small n_p.

This is further demonstrated by the goodness of the fits by calculating the root mean square error for different values of n_p, see Supporting Figure S13. While the fit to a stretched exponential for $H = 10.5$ mJ/mm^2 yields $\gamma \approx 1$, the rmse values are similar for both models. For the two highest fluences, strong deviations appear with increasing n_p, demonstrating the need for using the KWW model of a stretched exponential to model the data.

The KWW exponents γ extracted from $C(n_p, n_p + n)$ are shown in Supporting Figure S14 for the highest fluences probed. With increasing n_p, γ decreases reflecting increasing dynamical

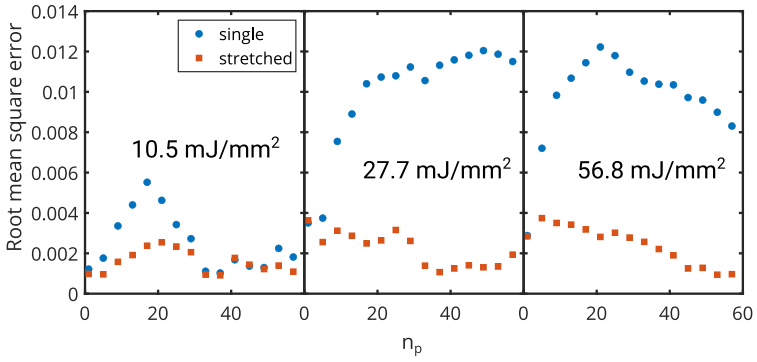

Supporting Figure S13. Root mean square errors of the fits to the single and stretched exponentials.

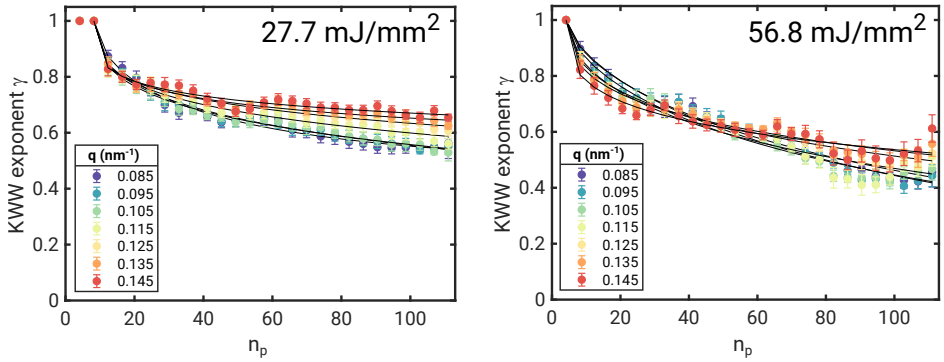

Supporting Figure S14. KWW exponents for $H = 27.7$ mJ/mm^2 (left) and $H = 56.8$ mJ/mm^2 (right) as a function of n_p for some q values.

heterogeneities. In this case the correlation function for different experimental times t_e becomes

$$g_2(t_e,\tau) = 1 + \frac{1}{V}\int_V \exp\left(-q^2 \frac{k_B T_{\text{eff}}(V',t_e,\tau)}{6\pi R \eta_{\text{eff}}(T_{\text{eff}}(V',t_e,\tau))}\tau\right) \mathrm{d}V', \tag{13}$$

with the sample volume V exposed to the beam, particle radius R, and effective viscosity η_{eff}. This integral leads to an effective broadening of g_2 with increasing differences in effective temperature T_{eff}.

The q-dependence of γ is shown in Supporting Figure S15 for three different values of n_p. In general, γ slightly decreases with increasing q at large n_p (here shown for $n_p = 100$). This indicates a higher degree of heterogeneity at large q corresponding to shorter length scales and suggests a larger impact of temperature heterogeneity at short length scales. This follows our model, assuming larger temperature differences closer to the particles' surface. At lower n_p values, the q-dependence appears to be different, e.g., γ increases with q for both fluences as shown for $n_p = 12$. This behavior is found in the regime where all diffusion models fail to explain the diffusivity data ($n_p < 20$, see Fig. 4c) and may thus be a fingerprint of the break-down of the Stokes-Einstein relation where the

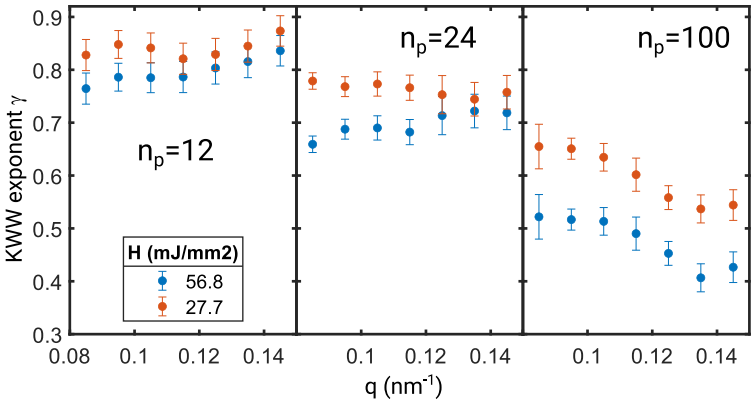

Supporting Figure S15. KWW exponents for the two highest fluences as function of q for three values of n_p.

nanoparticles move faster than expected from their and the solvent temperature – thus leading to increased heterogeneity on longer length scales. With further increasing n_p, the q-dependence of the KWW exponents changes as discussed above. This happens at different n_p for the two fluences, as highlighted for $n_p = 24$ in Supporting Figure V C. Here, the data at $H = 56.8$ mJ/mm^2 still increases with q, while γ is constant for $H = 27.7$ mJ/mm^2. Note that the differences between at different q-values are generally weak. Furthermore, with increasing n_p, and thus increasing relaxation rates, we are able to observe only the long-time tails of the correlation function leading to larger error bars for γ.

[1] A. P. Mancuso, A. Aquila, L. Batchelor, R. J. Bean, J. Bielecki, G. Borchers, K. Doerner, K. Giewekemeyer, R. Graceffa, O. D. Kelsey, Y. Kim, H. J. Kirkwood, A. Legrand, R. Letrun, B. Manning, L. L. Morillo, M. Messerschmidt, G. Mills, S. Raabe, N. Reimers, A. Round, T. Sato, J. Schulz, C. S. Takem, M. Sikorski, S. Stern, P. Thute, P. Vagovič, B. Weinhausen, and T. Tschentscher, The single particles, clusters and biomolecules and serial femtosecond crystallography instrument of the european XFEL: initial installation, Journal of Synchrotron Radiation **26**, 660 (2019).

[2] D. Boukhelef, J. Szuba, K. Wrona, and C. Youngman, Software development for high speed data recording and processing, in *14th International Conference on Accelerator & Large Experimental Physics Control Systems (ICALEPCS2013)* (2013).

[3] A. Allahgholi, J. Becker, A. Delfs, R. Dinapoli, P. Goettlicher, D. Greiffenberg, B. Henrich, H. Hirsemann, M. Kuhn, R. Klanner, A. Klyuev, H. Krueger, S. Lange, T. Laurus, A. Marras, D. Mezza, A. Mozzanica, M. Niemann, J. Poehlsen, J. Schwandt, I. Sheviakov, X. Shi, S. Smoljanin, L. Steffen, J. Sztuk-Dambietz, U. Trunk, Q. Xia, M. Zeribi, J. Zhang, M. Zimmer, B. Schmitt, and H. Graafsma, The adaptive gain integrating pixel detector at the european XFEL, Journal of Synchrotron Radiation **26**, 74 (2019).

[4] J. W. Goodman, *Speckle Phenomena in Optics* (Roberts and Company Publishers, 2006).

[5] L. Li, P. Kwaśniewski, D. Orsi, L. Wiegart, L. Cristofolini, C. Caronna, and A. Fluerasu, Photon statistics and speckle visibility spectroscopy with partially coherent x-rays, Journal of Synchrotron Radiation **21**, 1288 (2014).

[6] P. Falus, L. B. Lurio, and S. G. J. Mochrie, Optimizing the signal-to-noise ratio for x-ray photon correlation spectroscopy, Journal of Synchrotron Radiation **13**, 253 (2006).

[7] A. Madsen, A. Fluerasu, and B. Ruta, Structural dynamics of materials probed by x-ray photon correlation spectroscopy, in *Synchrotron Light Sources and Free-Electron Lasers* (Springer International Publishing, 2018) pp. 1–30.

[8] C. Gutt, P. Wochner, B. Fischer, H. Conrad, M. Castro-Colin, S. Lee, F. Lehmkühler, I. Steinke, M. Sprung, W. Roseker, D. Zhu, H. Lemke, S. Bogle, P. H. Fuoss, G. B. Stephenson, M. Cammarata, D. M. Fritz, A. Robert, and G. Grübel, Single shot spatial and temporal coherence properties of the SLAC linac coherent light source in the hard x-ray regime, Phys. Rev. Lett. **108**, 024801 (2012).

[9] F. Lehmkühler, C. Gutt, B. Fischer, M. A. Schroer, M. Sikorski, S. Song, W. Roseker, J. Glownia, M. Chollet, S. Nelson, K. Tono, T. Katayama, M. Yabashi, T. Ishikawa, A. Robert, and G. Grübel, Single shot coherence properties of the free-electron laser SACLA in the hard x-ray regime, Sci. Rep. **4**, 5234 (2014).

[10] D. L. Abernathy, G. Grübel, S. Brauer, I. McNulty, G. B. Stephenson, S. G. J. Mochrie, A. R. Sandy, N. Mulders, and M. Sutton, Small-angle x-ray scattering using coherent undulator radiation at the ESRF, Journal of Synchrotron Radiation **5**, 37 (1998).

[11] S. O. Hruszkewycz, M. Sutton, P. H. Fuoss, B. Adams, S. Rosenkranz, K. F. Ludwig, W. Roseker, D. Fritz, M. Cammarata, D. Zhu, S. Lee, H. Lemke, C. Gutt, A. Robert, G. Grübel, and G. B. Stephenson, High contrast x-ray speckle from atomic-scale order in liquids and glasses, Phys. Rev. Lett. **109**, 185502 (2012).

[12] K. Yun, S. Kim, D. Kim, M. Chung, W. Jo, H. Hwang, D. Nam, S. Kim, J. Kim, S.-Y. Park, K. S. Kim, C. Song, S. Lee, and H. Kim, Coherence and pulse duration characterization of the PAL-XFEL in the hard x-ray regime, Sci. Rep. **9**, 3300 (2019).

[13] R. Alonso-Mori, C. Caronna, M. Chollet, R. Curtis, D. S. Damiani, J. Defever, Y. Feng, D. L. Flath, J. M. Glownia, S. Lee, H. T. Lemke, S. Nelson, E. Bong, M. Sikorski, S. Song, V. Srinivasan, D. Stefanescu, D. Zhu, and A. Robert, The x-ray correlation spectroscopy instrument at the linac coherent light source, Journal of Synchrotron Radiation **22**, 508 (2015).

[14] D. Rings, R. Schachoff, M. Selmke, F. Cichos, and K. Kroy, Hot brownian motion, Phys. Rev. Lett. **105**, 090604 (2010).

[15] T. Gao and B. P. Jelle, Thermal conductivity of amorphous silica nanoparticles, J. Nanopart. Res. **21**, 108 (2019).

[16] J. Kestin, M. Sokolov, and W. A. Wakeham, Viscosity of liquid water in the range -8 °c to 150 °c, J. Phys. Chem. Ref. Data **7**, 941 (1978).